ROYAL SOCIETY
OF CHEMISTRY

PAPER

Check for updates

Enhanced photocatalytic hydrogen evolution by polyiodide-boosted electron transport and Pt–Ag alloy active sites in conductive polymer-based core–shell photocatalysts

Wenyan Zhang, [ID] *[a] Chaoqun Jiang,[b] Weidong Tao,[a] Yihan Wang,[a] Hangmin Guan [ID] [a] and Lingyun Hao[a]

The photocatalytic hydrogen evolution reaction (HER) represents a promising route for sustainable solar-to-hydrogen conversion; however, practical implementation is often constrained by inefficient charge transport and high noble-metal requirements. Here, we report a core–shell photocatalyst, $Fe_3O_4@PPy@Pt/Ag@I$, designed with a sustainability-oriented strategy that simultaneously addresses three critical challenges: resource-efficient use of noble metals, enhanced charge-transport efficiency, and operational recyclability. The *in situ* formation of Pt–Ag alloy nanodots reduces reliance on pure Pt while retaining high catalytic activity, improving noble-metal utilization efficiency. Polyiodide species (I_3^- and I_5^-) embedded within the polypyrrole (PPy) matrix facilitate efficient electron transport. The synergistic combination of polyiodide-assisted charge transfer and Pt–Ag alloy-mediated proton reduction enhances charge separation, prolongs carrier lifetimes, and accelerates HER kinetics, resulting in a 6.2-fold increase in the hydrogen-evolution rate and substantially improved Pt mass activity relative to $Fe_3O_4@PPy@Pt$. In addition, the magnetic Fe_3O_4 core enables facile recovery and reuse of the catalyst, demonstrating a cost-effective and sustainability-driven approach for conductive polymer-based photocatalytic hydrogen production.

Sustainability spotlight

The urgent need for clean, sustainable energy has intensified interest in hydrogen as a zero-carbon fuel, yet efficient photocatalytic hydrogen production remains a major challenge. This study enhances solar-driven hydrogen evolution by coupling conductive polymer-based photocatalysts with iodine-mediated electron transport regulation and Pt-Ag alloy active sites. This synergistic strategy achieves a 6.2-fold increase in hydrogen production efficiency. The approach is low-cost, environmentally friendly, and scalable, offering a promising pathway to advance green hydrogen technologies. It directly supports SDG 7 (Affordable and Clean Energy) and SDG 13 (Climate Action), providing practical solutions for clean energy generation and accelerating the transition to a low-carbon, sustainable future.

1. Introduction

In recent years, global energy challenges and environmental concerns arising from excessive fossil fuel consumption have underscored the urgent need for sustainable energy carriers. Hydrogen, with its high gravimetric energy density and carbon-free combustion, has emerged as a promising clean fuel. Among various production routes, solar-driven photocatalytic water splitting offers an attractive pathway for sustainable hydrogen generation. Nevertheless, practical efficiencies remain low due to limited charge-carrier separation and sluggish surface proton-reduction kinetics.[1,2] Effective photocatalytic hydrogen evolution therefore requires not only rapid charge transport and suppressed electron–hole recombination, but also catalytic sites with optimized hydrogen adsorption–desorption energetics to sustain fast reaction kinetics.[3–7]

Conductive polymers have attracted significant attention as platforms for photocatalytic and photoelectrochemical applications owing to their tunable electrical conductivity, structural flexibility, and solution processability. Among them, polypyrrole (PPy) is particularly appealing because of its extended π-conjugated backbone, which enables intra- and interchain charge transport *via* hopping and tunneling mechanisms, facilitating rapid electron migration and improved charge separation.[8,9] Furthermore, the electrical conductivity and electronic structure of PPy can be tailored through controlled doping, providing a versatile approach to regulate charge

[a]College of Material Engineering, Jinling Institute of Technology, Nanjing 211169, China. E-mail: wiseyanyan@jit.edu.cn; Fax: +86-25-86188966; Tel: +86-25-86188966
[b]College of Architecture Engineering, Jinling Institute of Technology, Nanjing 211169, China

transport in photocatalytic systems.[10] Despite these advantages, the intrinsic charge mobility of pristine PPy remains insufficient for high-efficiency HER, highlighting the need for further electronic-structure engineering.

Iodine doping has long been recognized as an effective strategy to enhance the conductivity of π-conjugated polymers, including polyaniline (PANI), polyacetylene (PA), and polythiophene, by extracting electrons from the polymer backbone and generating mobile charge carriers such as polarons and bipolarons.[11–14] This often leads to the formation of polyiodide species (e.g., I_3^- and I_5^-), which interact with the conjugated framework to reduce charge-transfer barriers and promote electron delocalization.[15,16] While these effects have been extensively studied in electronic and electrochemical applications, the role of polyiodide-assisted charge transport in the PPy-based photocatalytic HER, including its influence on charge migration and long-term operational stability, remains underexplored.[17–19] Understanding these effects is essential for designing PPy-based photocatalysts with both higher efficiency and improved sustainability.

Beyond charge transport, the sustainability of photocatalytic hydrogen evolution critically depends on the efficient use of noble-metal catalytic sites. Platinum is widely regarded as the benchmark catalyst for hydrogen evolution due to its near-optimal hydrogen adsorption free energy. However, its high cost and limited availability present significant barriers to scalable application.[20] Traditional strategies to improve activity, such as increasing Pt loading or surface exposure, conflict with sustainability objectives. Alloying Pt with more abundant metals has emerged as an effective approach to modulate the electronic structure, optimize hydrogen binding, and reduce noble-metal demand without compromising catalytic performance.[21] Among potential alloying elements, silver (Ag) is an attractive candidate due to its weak hydrogen affinity, favorable electronic interaction with Pt, and ability to modify the Pt d-band center.[22,23] Besides, Ag nanostructure incorporation can enhance light–matter interactions for further enhancement of photocatalytic efficiency while improving noble-metal utilization efficiency during the HER process.[24]

Efficient photocatalyst design therefore requires the simultaneous optimization of charge transport, noble-metal utilization, and catalyst recoverability. Enhancing charge transport *via* dopants or redox mediators can introduce instability or leaching, while increasing noble-metal loading improves activity at the expense of cost and sustainability. These trade-offs highlight the challenge of achieving high activity alongside operationally robust, resource-efficient catalyst structures. Accordingly, a key design objective is to integrate efficient charge-transport regulation with noble-metal-efficient active sites within a structurally recoverable architecture, thereby addressing both performance and sustainability considerations.

Guided by these principles, we report a core–shell Fe_3O_4@PPy@Pt/Ag@I photocatalyst that synergistically combines polyiodide-assisted charge transport with Pt–Ag alloy active sites confined within a magnetically recyclable polymer matrix. Polyiodide species embedded in the PPy network facilitate electron transport *via* stabilized charge-transfer interactions, while Pt–Ag alloy nanodots optimize hydrogen adsorption–desorption energetics and interfacial electron transfer. This dual-regulation strategy enables enhanced HER activity, improved noble-metal utilization efficiency, and facile catalyst recovery, providing a sustainability-oriented design framework for conductive-polymer-based photocatalytic systems.

2. Experimental

A core–shell structured catalyst was rationally designed to test the hypothesis that iodine doping can enhance electron transport in π-conjugated polymers, thereby improving photocatalytic hydrogen evolution performance.

2.1. Core–shell photocatalyst Fe_3O_4@PPy@Pt decorated with Pt as active sites

Monodispersed Fe_3O_4 microspheres were fabricated *via* a hydrothermal method. Briefly, 0.54 g of $FeCl_3 \cdot 6H_2O$, 1.2 g of sodium citrate, and 0.2 g of urea were dissolved in 40 mL of distilled water, followed by the addition of 0.2 g of sodium polyacrylate (PAAS) under stirring. The solution was transferred into a 50 mL Teflon-lined autoclave and heated at 200 °C for 12 h. The resulting Fe_3O_4 microspheres were magnetically separated, washed with deionized water and ethanol, and dried under vacuum at 60 °C.

To prepare Fe_3O_4@PPy core–shell structures, 0.2 g of Fe_3O_4 microspheres and 0.05 g of polyvinylpyrrolidone (PVP) were ultrasonically dispersed in 40 mL of deionized water, followed by adding 0.108 g $FeCl_3$ and 50 μL pyrrole under intense ultrasonication for 2-h polymerization. The resulting Fe_3O_4@PPy composite was magnetically collected, washed, and dried. Pt nanodots were introduced by a microwave-assisted deposition method. In a typical procedure, 0.2 g of Fe_3O_4@PPy and 0.05 g of PVP were dispersed in 20 mL of deionized water and mixed with 20 mL of ethylene glycol. Then, 1 mL of K_2PtCl_6 solution (2 mg per mL Pt) was added, and the mixture was irradiated under an 800 W microwave source for 5 min under reflux. The product (Fe_3O_4@PPy@Pt) was magnetically separated, washed, and dried.

2.2. Preparation of Fe_3O_4@PPy@Ag@I

The as-prepared Fe_3O_4@PPy was first washed with deionized water by magnetic separation after dispersion in a PVP aqueous solution (1 mg mL^{-1}). Then, 1 mg of purified Fe_3O_4@PPy was redispersed in 20 mL of deionized water. Subsequently, 100 μL of $AgNO_3$ solution (0.1 M) was added dropwise under stirring, followed by the dropwise addition of 100 μL of KI solution (0.1 M), resulting in the formation of Fe_3O_4@PPy@Ag@I.

2.3. Core–shell photocatalyst Fe_3O_4@PPy@Pt/Ag@I (Pt/Ag alloy as active sites)

Iodine species incorporation and Pt–Ag alloy active site formation were realized through light-induced reduction. Briefly, 1 mg Fe_3O_4@PPy@Ag@I was dispersed in 100 mL 10% (v/v) TEOA aqueous solution *via* 30-min ultrasonication. After

30 min, 70 mg eosin Y (EY) was introduced. The suspension was deaerated by Ar bubbling for 30 min and then irradiated with a 300 W Xe lamp (equipped with a 420 nm cut-off or band-pass filter) for 60 min in a sealed 100 mL Pyrex flask. During this irradiation process, metallic Pt was *in situ* deposited on Fe_3O_4@PPy@Ag@I to form Fe_3O_4@PPy@Pt/Ag@I, which has Pt/Ag alloy active sites.

The incorporation of iodine species and the formation of Pt–Ag alloy active sites were achieved *via* a light-induced reduction process. Briefly, 1 mg of Fe_3O_4@PPy@Ag@I was dispersed in 100 mL of a 10% (v/v) aqueous triethanolamine (TEOA) solution by ultrasonication for 30 min. Then, 70 mg of eosin Y (EY) was added. The suspension was deaerated by Ar bubbling for 30 min and subsequently irradiated with a 300 W Xe lamp (equipped with a 420 nm cutoff or band-pass filter) for 60 min in a sealed 100 mL Pyrex reactor. During irradiation, Pt was *in situ* photo-deposited onto Fe_3O_4@PPy@Ag@I, forming Fe_3O_4@PPy@Pt/Ag@I with Pt–Ag alloy active sites.

2.4. Characterization

Photocatalytic hydrogen evolution experiments were carried out in a sealed 120 mL Pyrex reactor under ambient conditions at room temperature. Typically, 1 mg of Fe_3O_4@PPy@Pt/Ag@I photocatalyst was dispersed in 20 mL of an aqueous solution containing 10% (v/v) triethanolamine (TEOA) and 1×10^{-3} M eosin Y. The suspension was deaerated by Ar bubbling for 30 min and then irradiated using a 300 W Xe lamp equipped with a 420 nm cutoff filter. The amount of evolved hydrogen was quantified by gas chromatography (Agilent 6820, TCD, Ar carrier gas).

Monochromatic photocatalytic hydrogen evolution measurements were performed at 420, 520, and 550 nm. The apparent quantum yield (AQY) at each wavelength was calculated using the following equation:

$$\text{AQY (\%)} = (2 \times \text{number of evolved H}_2 \text{ molecules} \times 100\%)/ \text{(number of incident photons)}$$

The Pt mass activity was calculated based on the nominal Pt loading introduced during photodeposition. Due to the low Pt content and alloyed nature of the Pt–Ag nanodots, direct quantification of actual Pt content may introduce additional uncertainty. Importantly, the same normalization method was consistently applied to all Pt-containing samples to ensure reliable relative performance comparison.

Photocatalytic stability and recyclability were evaluated by consecutive cycling experiments under identical reaction conditions. After each photocatalytic cycle, the catalyst was recovered from the reaction suspension using an external magnetic field and reused for the subsequent cycle.

Photocurrent measurements were performed on a CHI660E workstation using a three-electrode configuration, with a Pt wire as the counter electrode, a saturated calomel electrode (SCE) as the reference electrode, and an FTO-supported catalyst as the working electrode. Measurements were conducted under

a 300 W Xe lamp with a 420 nm cut-off filter in an electrolyte containing 10% TEOA and 10^{-3} M EY.

Structural and optical characterization studies were carried out using TEM (Tecnai G2-F30, 300 kV), XRD (Rigaku B/Max-RB, Cu Kα), XPS (VG ESCALAB210), and photoluminescence spectroscopy (Horiba TCSPC system, 460 nm nano-LED excitation). Electrical conductivity was measured using a Keithley 4200 system with a two-probe configuration at room temperature in air.

The electrochemically active surface area (ECSA) was estimated from the double-layer capacitance (C_{dl}) using the relation $\text{ECSA} = C_{dl}/C_s$. The C_{dl} values were obtained from cyclic voltammetry in a non-faradaic region at different scan rates. For nanostructured or porous catalysts, reported C_s values typically range from 20 to 60 μF cm^{-2}.[25,26] Here, an average value of 40 μF cm^{-2} was adopted. Using a higher C_s value (*e.g.*, 60 μF cm^{-2}) would reduce the absolute ECSA values by approximately 30–35%, but would not affect the observed trends. This approach therefore provides a reliable basis for relative comparison of the electrochemically active surface area among the different catalysts.

3. Results and discussion

3.1. Structural characterization of photocatalysts

As shown in Fig. 1(a and b), the synthesized Fe_3O_4@PPy@Pt/Ag@I exhibits a uniform spherical morphology with a continuous polypyrrole (PPy) shell of approximately 50–100 nm in thickness. STEM-EDS elemental mapping (Fig. 2) further confirms the homogeneous distribution of C derived from the PPy framework (Fig. 2(a2)). The Fe and O signals (Fig. 2(a3 and a4)) correspond to the Fe_3O_4 microsphere core, indicating that the Fe_3O_4 particles are fully encapsulated by the conductive PPy shell. Notably, iodine is also uniformly distributed throughout the PPy layer (Fig. 2(a5)). In agreement with this observation, the I 3d XPS spectrum (Fig. 2(b)) displays characteristic components of I_3^- and I_5^-, confirming the incorporation of polyiodide species into the PPy shell of Fe_3O_4@PPy@Pt/Ag@I.

Numerous nanodots with diameters of approximately 3–6 nm are uniformly distributed within and on the surface of the PPy shell (Fig. 1(c)). The HRTEM image (Fig. 1(d)) reveals clear lattice fringes with interplanar spacings of 0.227–0.229 nm, which lie between the (111) planes of metallic Ag (0.236 nm) and Pt (0.226 nm). This intermediate spacing strongly suggests the formation of Pt–Ag alloy nanodots through the light-induced deposition process. Consistently, STEM-EDS elemental mapping shows highly overlapping distributions of Pt and Ag throughout the PPy shell (Fig. 2(a6 and a7)). The Ag 3d and Pt 4f XPS spectra (Fig. 2(c and d)) further confirm that both Ag and Pt remain in their zero-valent metallic states after photodeposition.

To further elucidate the electronic interaction and alloying behavior between Pt and Ag, the Ag 3d XPS spectrum of Fe_3O_4@PPy@Pt/Ag@I was compared with that of Fe_3O_4@PPy@Ag@I, while the Pt 4f spectra were compared with that of Fe_3O_4@PPy@Pt. These comparative analyses provide compelling evidence for the formation of the Pt–Ag alloy. As shown in
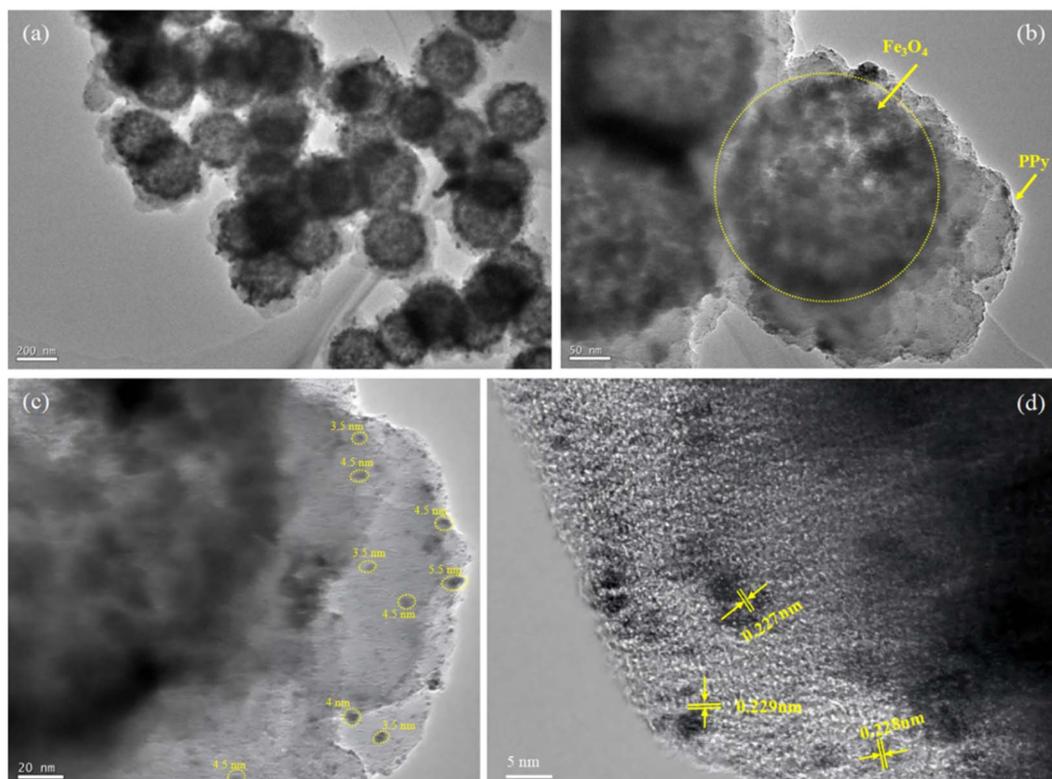
Fig. 1 (a–c) TEM images of Fe_3O_4@PPy@Pt/Ag@I at different magnifications. (d) HRTEM image of Fe_3O_4@PPy@Pt/Ag@I showing Pt–Ag alloy nanodots.

Fig. 2(c), the Ag 3d peaks of Fe_3O_4@PPy@Pt/Ag@I exhibit a noticeable positive (blue) shift relative to Fe_3O_4@PPy@Ag@I, indicating a decreased electron density on Ag. Conversely, the Pt 4f peaks of Fe_3O_4@PPy@Pt/Ag@I display a negative (red) shift accompanied by reduced intensity compared with those of Fe_3O_4@PPy@Pt (Fig. 2(d)). These opposite binding-energy shifts—Ag 3d to higher and Pt 4f to lower energies—are consistent with electron transfer from Ag to Pt, arising from their electronegativity difference (Pt: 2.28; Ag: 1.93) and d-band hybridization during alloy formation. This charge redistribution increases the electron density on Pt while decreasing that on Ag, providing strong evidence for Pt–Ag alloying rather than simple physical mixing. Together, with the intermediate lattice spacing in HRTEM (Fig. 1(d)) and the uniform Pt/Ag co-distribution in STEM-EDS (Fig. 2(a6 and a7)), these results conclusively demonstrate the *in situ* formation of Pt–Ag alloy nanodots within the PPy shell.

3.2. Photocatalytic performance of photocatalysts

With the introduction of iodine species and Pt–Ag alloy nanodots into Fe_3O_4@PPy, the hydrogen evolution efficiency was enhanced by up to 6.2 fold, increasing from 55 349 μmol per g Pt to 344 279 μmol per g Pt, as shown in Fig. 3(a). As summarized in Table 1, the Pt mass activity of Fe_3O_4@PPy@Pt/Ag@I reaches 172 139.5 μmol per h per g Pt, which is markedly higher than that of Fe_3O_4@PPy@Pt (27 674.5 μmol per h per g Pt). In contrast, the control sample Fe_3O_4@PPy@Ag@I, which

contains Ag–I species but no Pt, exhibits negligible hydrogen evolution activity (see Fig. 3(a)). This result indicates that Ag–I species alone cannot serve as effective HER active sites, but instead play a cooperative role when integrated with Pt in the alloyed Fe_3O_4@PPy@Pt/Ag@I system. Collectively, these results suggest that the superior HER activity of Fe_3O_4@PPy@Pt/Ag@I originates from the synergistic interaction between Pt–Ag alloy active sites and polyiodide species, rather than from increased Pt loading, thereby directly addressing a key sustainability constraint related to noble-metal utilization.

Consistent with its enhanced photocatalytic performance, Fe_3O_4@PPy@Pt/Ag@I delivers a photocurrent density of 0.6 μA cm^{-2}, which is more than three times higher than that of Fe_3O_4@PPy@Pt (Fig. 3(b)). This improvement indicates more efficient photoinduced charge separation and interfacial electron transfer, arising from the combined effects of polyiodide-mediated charge transport and Pt–Ag alloy active sites. The hydrogen evolution of Fe_3O_4@PPy@Pt/Ag@I was further evaluated under monochromatic light irradiation to determine its apparent quantum yield (AQY) values. As shown in Fig. 3(c), AQY values of 12.5%, 8.8%, and 3.9% were obtained at 420 nm, 520 nm and 550 nm, respectively.

Furthermore, Fig. 3(d) illustrates the effect of the Ag/Pt ratio on the hydrogen evolution activity of Fe_3O_4@PPy@Pt/Ag@I, revealing that the catalytic performance is optimized at an Ag/Pt ratio of 6 : 1. This observation further supports the role of the Pt–Ag alloy as the primary active site. Considering that silver
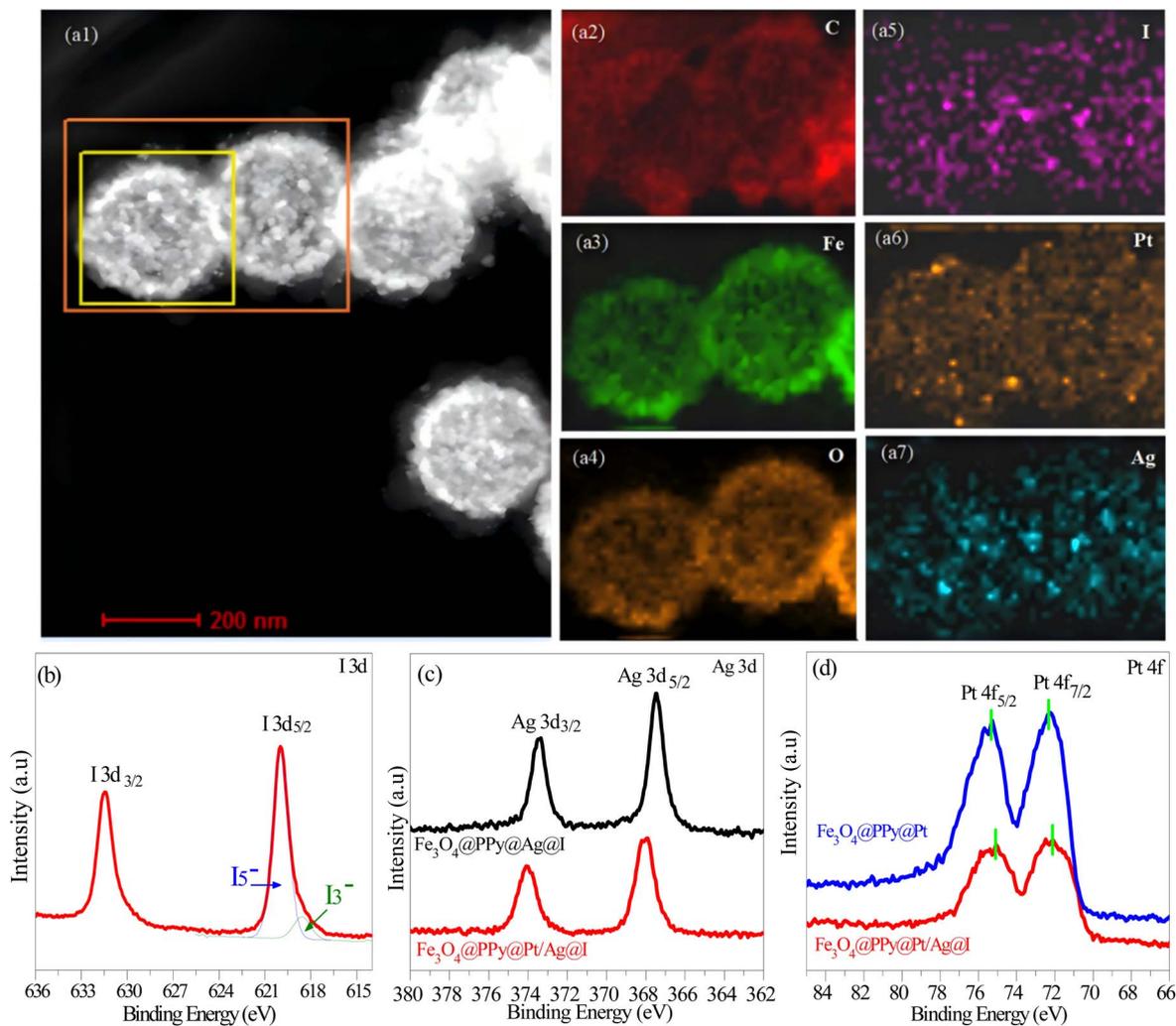
Fig. 2 (a) STEM–EDS elemental mapping of Fe$_3$O$_4$@PPy@Pt/Ag@I: (a1) HAADF image; (a2–a7) C, Fe, O, I, Pt and Ag, respectively. (b) I 3d XPS spectrum of Fe$_3$O$_4$@PPy@Pt/Ag@I. (c) Ag 3d XPS spectra of Fe$_3$O$_4$@PPy@Ag@I and Fe$_3$O$_4$@PPy@Pt/Ag@I. (d) Pt 4f XPS spectra of Fe$_3$O$_4$@PPy@Pt and Fe$_3$O$_4$@PPy@Pt/Ag@I.

is significantly less expensive than platinum, the incorporation of Ag into Pt-based catalysts provides an effective strategy for reducing catalyst cost while retaining high catalytic efficiency.

To gain deeper insight into the origin of the enhanced hydrogen evolution activity of Fe$_3$O$_4$@PPy@Pt/Ag@I, a series of characterization studies, including transient photocurrent measurements, current–voltage (I–V) analysis, linear sweep voltammetry (LSV), and photoluminescence (PL) spectroscopy, were conducted, which collectively provide mechanistic insights into how polyiodide species and alloyed active sites contribute to enhanced charge transfer and catalytic kinetics.

In Fig. 4(a), the I–V curves indicate that Fe$_3$O$_4$@PPy@Pt/Ag@I exhibits a higher current response over the entire voltage range compared with Fe$_3$O$_4$@PPy@Pt, suggesting an increased effective charge carrier density and improved electron-transport efficiency. This enhancement is likely associated with the interaction between polyiodides species and the π-conjugated PPy shell, consistent with previous reports on iodide-assisted charge transport in conjugated systems.[27]

The incorporation of I$_3^-$/I$_5^-$ polyiodides can facilitate charge transport by forming charge-transfer interactions with the π-conjugated PPy framework and enabling p-orbital-mediated electron hopping pathways, as schematically illustrated in Fig. 4(b). Collectively, these effects are expected to accelerate charge migration and suppress carrier recombination, thereby contributing to enhanced photocatalytic hydrogen-evolution performance.

The hydrogen evolution performance of the photocatalysts was further evaluated via linear sweep voltammetry (LSV). As shown in Fig. 5, Fe$_3$O$_4$@PPy@Pt/Ag@I exhibited a markedly lower onset potential of −0.58 V, compared with −0.65 V for Fe$_3$O$_4$@PPy@Pt, indicating more favorable HER kinetics. This improvement can be rationalized by the formation of Pt–Ag alloy active sites, which can modulate the local electronic structure by downshifting the Pt d-band center and thereby optimizing the hydrogen adsorption free energy (ΔG_{H*}), leading to a more balanced H* adsorption–desorption process.[28–30] Thereby, the surface proton reduction kinetics are facilitated,

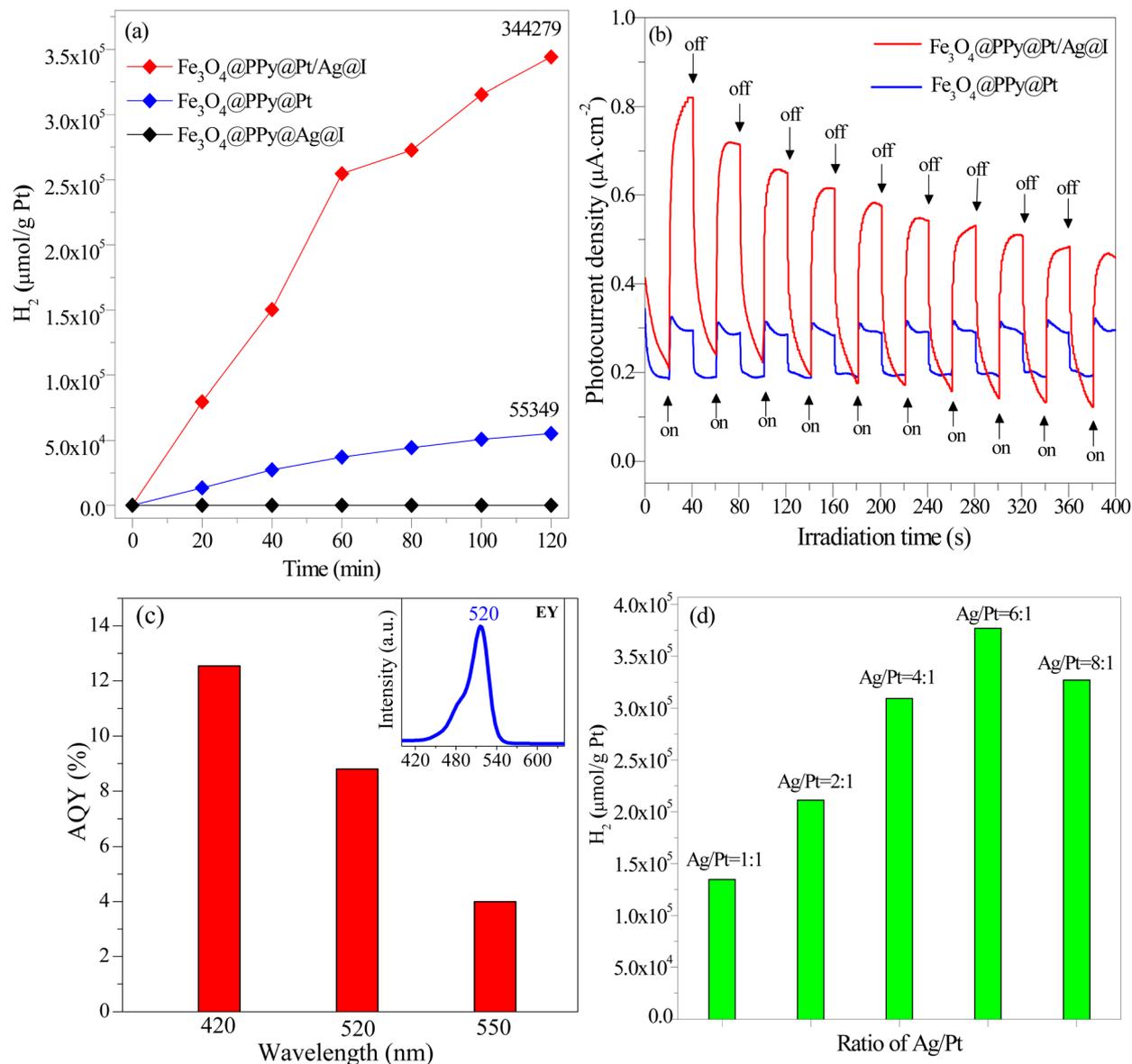**Fig. 3** (a) Time courses of H_2 evolution over $Fe_3O_4@PPy@Pt/Ag@I$, $Fe_3O_4@PPy@Pt$, and $Fe_3O_4@PPy@Ag@I$. (b) Transient photocurrent responses of $Fe_3O_4@PPy@Pt/Ag@I$ and $Fe_3O_4@PPy@Pt$ (EY as the sensitizer in 20 mL of 10% (v/v) TEOA under visible-light irradiation, $\lambda \geq 420$ nm). (c) Apparent quantum yield (AQY) of $Fe_3O_4@PPy@Pt/Ag@I$, with the inset showing the UV-vis absorbance spectrum of the EY sensitizer. (d) Effect of the Ag/Pt ratio on the hydrogen evolution activity of $Fe_3O_4@PPy@Pt/Ag@I$.

Table 1 Hydrogen evolution performance of different photocatalysts

Photocatalyst	Hydrogen evolution (μmol per g Pt)	Pt mass activity (μmol per h per g Pt)
$Fe_3O_4@PPy@Pt$	55 349	27 674.5
$Fe_3O_4@PPy@Pt/Ag@I$	344 279	172 139.5

giving rise to a reduced overpotential for the HER. Moreover, the cathodic current density of $Fe_3O_4@PPy@Pt/Ag@I$ is approximately 2.3 times higher than that of $Fe_3O_4@PPy@Pt$, further suggesting enhanced charge-transfer efficiency and catalytic activity. This behavior may also be related to the

incorporation of polyiodide species within the π-conjugated PPy backbone, which promotes more efficient electron migration toward the alloyed active sites for proton reduction.

The photoluminescence (PL) spectra (Fig. 6) exhibited pronounced fluorescence quenching upon the introduction of $Fe_3O_4@PPy@Pt$ and $Fe_3O_4@PPy@Pt/Ag@I$ into the EY solution, indicating enhanced interfacial electron transfer from photo-excited EY to the photocatalyst surface. Notably, compared with $Fe_3O_4@PPy@Pt$, the $Fe_3O_4@PPy@Pt/Ag@I$ sample shows an additional blue shift of the emission peak to 518 nm. This spectral shift is consistent with the localized surface plasmon resonance (LSPR) effect introduced by Ag-containing nano-structures, which can modify the local electromagnetic field and
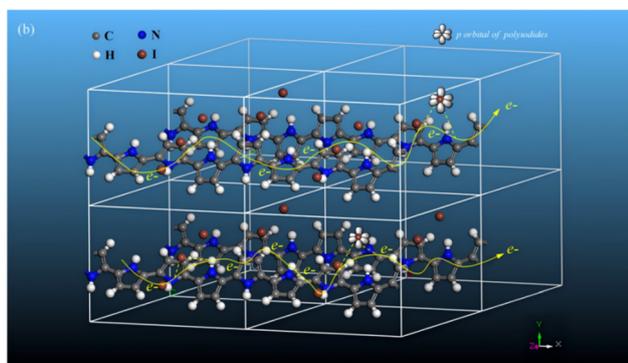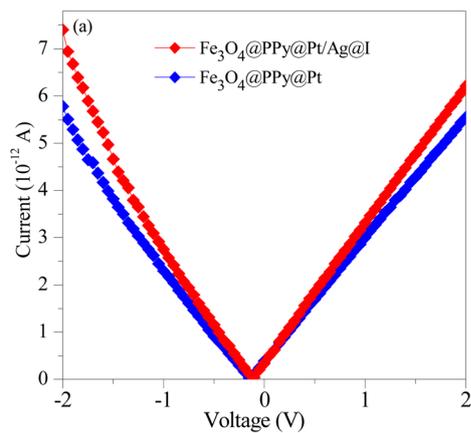
Fig. 4 (a) I–V characteristic curves of Fe$_3$O$_4$@PPy@Pt/Ag@I and Fe$_3$O$_4$@PPy@Pt. (b) Schematic of electron transportation and hopping through the iodide incorporated PPy chain.

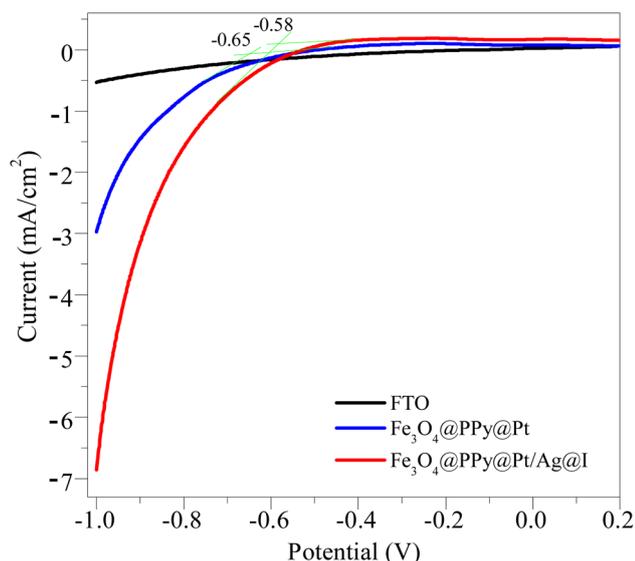Fig. 5 Linear sweep voltammetry (LSV) curves of Fe$_3$O$_4$@PPy@Pt/Ag@I and Fe$_3$O$_4$@PPy@Pt.

alter the photophysical environment of nearby EY molecules, thereby influencing their emission characteristics.[31,32]

Time-resolved fluorescence decay measurements further support the enhanced charge-transfer dynamics induced by the
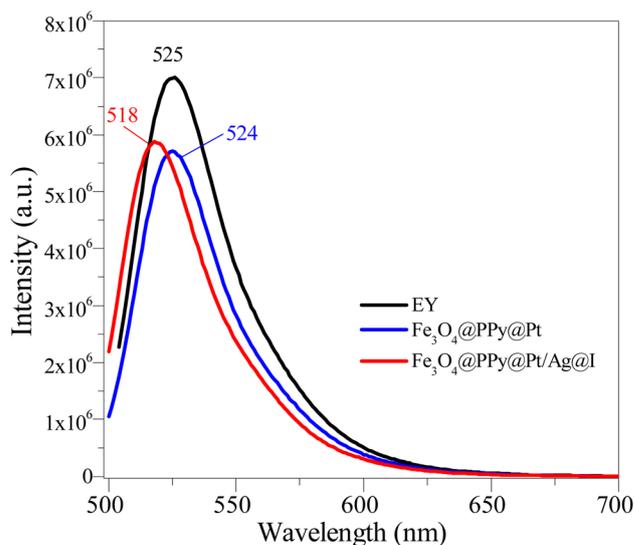

Fig. 6 Photoluminescence (PL) spectra of EY solution, EY + Fe$_3$O$_4$@PPy@Pt, and EY + Fe$_3$O$_4$@PPy@Pt/Ag@I under excitation at 520 nm (EY concentration: 1.0×10^{-5} M in 10% (v/v) TEOA aqueous solution).

incorporation of polyiodide species (I_3^-/I_3^-) and the formation of Pt–Ag alloy nanodots in the Fe$_3$O$_4$@PPy@Pt/Ag@I catalyst. The corresponding fluorescence decay lifetimes extracted from time-resolved PL measurements are summarized in Table 2. EY in TEOA solution exhibits a single-exponential decay behavior, characteristic of emission from monomeric EY molecules. Upon addition of Fe$_3$O$_4$@PPy@Pt, the decay profile evolves into a bi-exponential form, with lifetimes of 0.81 ns (short-lived component) and 1.41 ns (long-lived component), which can be attributed to interfacial interactions between photoexcited EY molecules, the π-conjugated PPy shell, and Pt active sites.

After further introducing polyiodide species and Pt–Ag alloy nanodots, the average fluorescence lifetimes increase to 1.28 ns and 2.75 ns, indicating more efficient charge separation and suppressed radiative recombination. Taken together, the observed fluorescence quenching and prolonged decay lifetimes indicate that the synergistic effects of polyiodide-assisted charge transport and Pt–Ag alloying promote more efficient charge separation and suppress carrier recombination, thereby contributing to enhanced hydrogen evolution performance.

Table 2 Fluorescence decay lifetimes of EY in the presence of different photocatalysts[a]

System	Lifetime (τ, ns)	Pre-exponential factors (B)	χ^2
EY	$\tau = 1.23$	$B = 0.0727$	1.00
Fe$_3$O$_4$@PPy@Pt	$\tau_1 = 0.81$	$B_1 = 0.048$	1.00
	$\tau_2 = 1.41$	$B_2 = 0.039$	
Fe$_3$O$_4$@PPy@Pt/Ag@I	$\tau_1 = 1.28$	$B_1 = 0.037$	1.00
	$\tau_2 = 2.75$	$B_2 = 0.026$	

[a] τ_1 and τ_2 correspond to the short- and long-lived fluorescence decay components obtained from biexponential fitting.
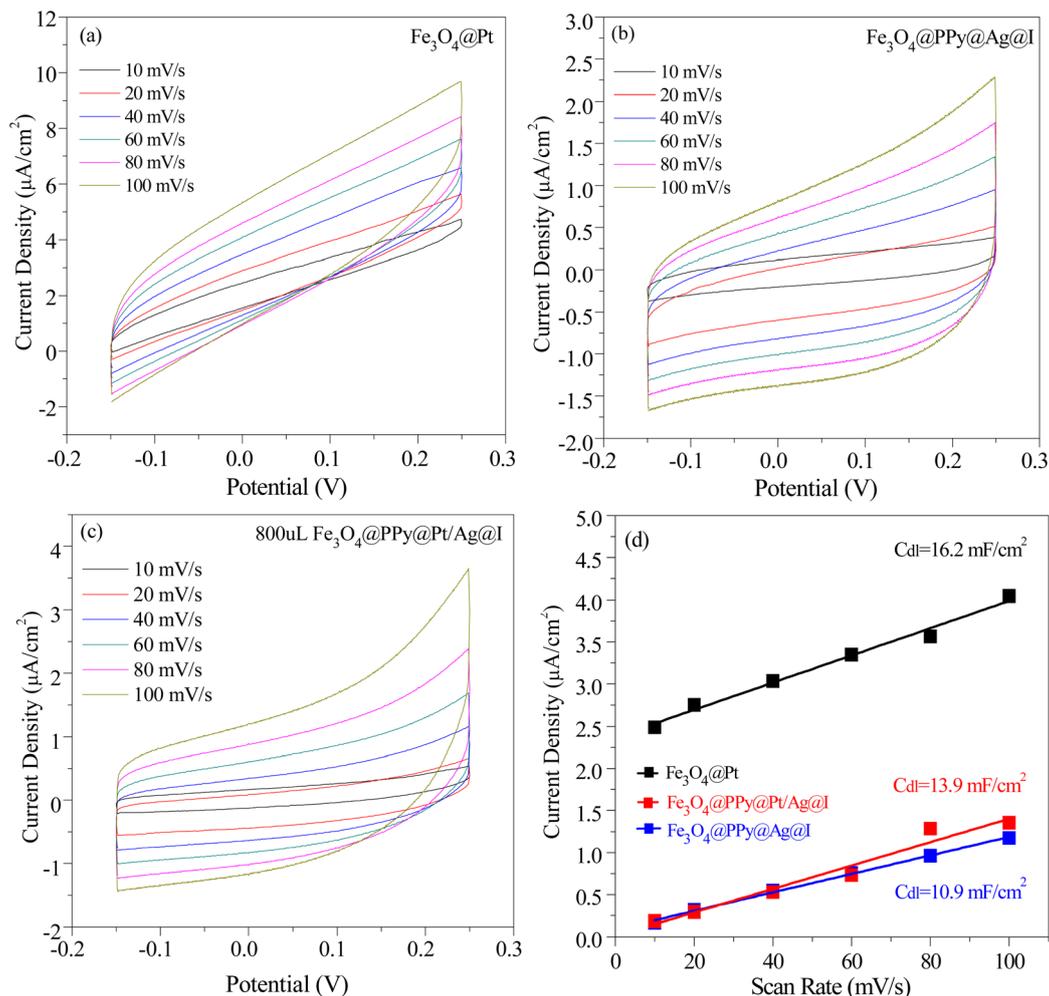
Paper

Fig. 7 Cyclic voltammetry (CV) curves collected in the non-faradaic region at different scan rates for (a) $Fe_3O_4@Pt$, (b) $Fe_3O_4@PPy@Ag@I$, and (c) $Fe_3O_4@PPy@Pt/Ag@I$. (d) Corresponding capacitive current density as a function of scan rate used for extracting the double-layer capacitance (C_{dl}).

Table 3 Double-layer capacitance (C_{dl}) and estimated electrochemically active surface area (ECSA) of different photocatalysts

Photocatalyst	C_{dl} (mF cm^{-2})	ECSA
$Fe_3O_4@Pt$	16.2	405
$Fe_3O_4@PPy@Ag@I$	10.9	272.5
$Fe_3O_4@PPy@Pt/Ag@I$	13.9	347.5

3.3. Electrochemical active surface area (ECSA) and role of electronic effects

To decouple the respective contributions of surface area and the electronic structure to the catalytic performance, the electrochemical active surface area (ECSA) of the photocatalysts was estimated using the double-layer capacitance (C_{dl}) method (Fig. 7), derived from cyclic voltammetry measurements collected in the non-faradaic potential region. The calculated ECSA values are summarized in Table 3. The pristine $Fe_3O_4@Pt$ microspheres exhibit a relatively high ECSA value of 405, which can be reasonably ascribed to the electrochemically accessible

surface enabled by the spherical Fe_3O_4 architecture composed of densely packed Fe_3O_4 nanocrystals with a rough surface texture (Fig. S8). This hierarchical morphology provides abundant anchoring sites for the high dispersion of Pt species, thereby contributing to the enlarged electrochemically accessible surface area.

Upon encapsulation of the Fe_3O_4 core with a conductive polypyrrole (PPy) shell followed by the incorporation of Ag and polyiodide species to form $Fe_3O_4@PPy@Ag@I$, the ECSA decreases to 272.5. This reduction suggests that the formation of the PPy shell and the Ag–I layer, while essential for constructing a synergistic interfacial structure, partially covers or fills the surface features of the original $Fe_3O_4@Pt$, resulting in a lower fraction of electrochemically accessible surface area. This observation further confirms that surface area is not the dominant factor governing the enhanced catalytic performance observed in the subsequent catalyst.

After the formation of Pt–Ag alloy active sites to generate the final $Fe_3O_4@PPy@Pt/Ag@I$ catalyst, the ECSA increases to 347.5. This partial recovery indicates that alloy formation
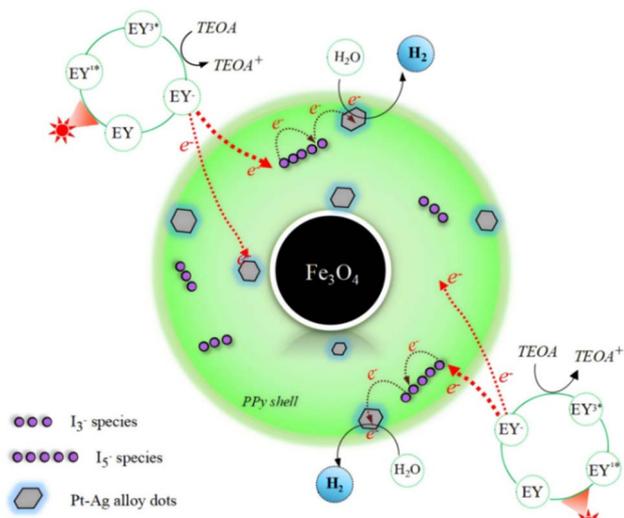
Scheme 1 Schematic illustration of the photocatalytic hydrogen evolution mechanism over Fe_3O_4@PPy@Pt/Ag@I.

facilitates the exposure of electrochemically accessible active sites and improves the intrinsic activity per site. More importantly, the fact that Fe_3O_4@PPy@Pt/Ag@I exhibits superior hydrogen evolution activity compared to pristine Fe_3O_4@Pt—despite possessing a lower ECSA—provides evidence that electronic structure modulation, rather than surface area, plays the dominant role in driving the observed activity enhancement. The optimized electronic environment, induced by the synergistic interplay between the Pt–Ag alloy and the polyiodide-modified PPy shell, promotes interfacial charge transfer and optimizes the adsorption energetics of reaction intermediates on the active sites.

3.4. Photocatalytic mechanism

Taken together, the ECSA analysis, photoelectrochemical measurements, and spectroscopic characterization consistently indicate that the enhanced hydrogen evolution activity of Fe_3O_4@PPy@Pt/Ag@I is predominantly governed by electronic structure modulation and interfacial charge-transfer dynamics rather than by surface area effects alone.

Based on the above analyses, a plausible photocatalytic hydrogen evolution mechanism over Fe_3O_4@PPy@Pt/Ag@I is proposed and illustrated in Scheme 1. Under visible-light irradiation, the photosensitizer EY absorbs photons and is promoted to its singlet excited state (EY^{1*}), which rapidly undergoes intersystem crossing to generate the triplet excited state (EY^{3*}). The excited EY^{3*} species is subsequently reductively quenched by triethanolamine (TEOA), yielding the $EY^{-\bullet}$ radical anion along with oxidized $TEOA^+$ species. The photo-excited electrons stored in $EY^{-\bullet}$ are then transferred to the Fe_3O_4@PPy@Pt/Ag@I photocatalyst through π–π interactions between EY molecules and the π-conjugated PPy shell. This interfacial electron injection enables effective spatial separation of photogenerated charge carriers and suppresses charge recombination. This behavior is well supported by the pronounced photoluminescence quenching observed upon the addition of Fe_3O_4@PPy@Pt/Ag@I (Fig. 6) and the prolonged fluorescence lifetimes summarized in Table 2, confirming efficient electron extraction from the excited EY sensitizer.

Within the PPy shell, the incorporated I_3^-/I_5^- polyiodide species act as effective charge-transfer mediators, facilitating electron migration along the conjugated polymer backbone and opening additional hopping pathways for charge transport. This behavior is further corroborated by electrochemical impedance spectroscopy (EIS) analysis. As shown in Fig. 8 and Table 4, the Nyquist plots reveal a pronounced decrease in charge-transfer resistance (R_2) upon polyiodide incorporation, indicating enhanced electrical conductivity of the PPy matrix.
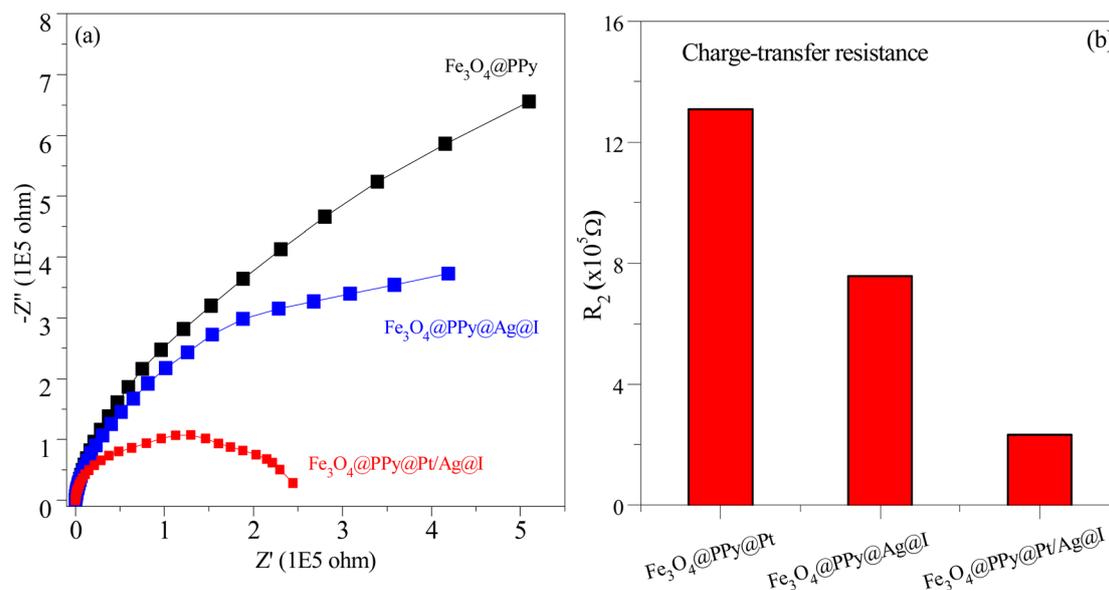

Fig. 8 (a) Nyquist plots and (b) charge-transfer resistance of different photocatalysts derived from EIS measurements.

Paper

Table 4 Charge-transfer resistance (R_2) of different photocatalysts obtained from Nyquist plot fitting

Photocatalyst	R_1	Q-Yo	Q-n	R_2	Chi
Fe_3O_4@PPy@Pt	3.23×10^1	1.09×10^{-5}	9.27×10^{-1}	1.31×10^6	1.96×10^{-3}
Fe_3O_4@PPy@Ag@I	5.57×10^1	1.15×10^{-5}	9.33×10^{-1}	7.57×10^5	5.23×10^{-3}
Fe_3O_4@PPy@Pt/Ag@I	4.39×10^1	9.69×10^{-6}	9.60×10^{-1}	2.32×10^5	1.31×10^{-3}

These results are consistent with the formation of charge-transfer complexes between polyiodide species and the π-conjugated PPy chains, which significantly promote interfacial electron transport from the photosensitizer to the catalytically active sites. The transferred electrons are subsequently delivered to the Pt–Ag alloy nanodots, where alloying-induced electronic modulation optimizes the hydrogen adsorption free energy (ΔG_{H*}) by achieving a more balanced H* adsorption–desorption process. As a result, proton reduction kinetics are accelerated, leading to the markedly enhanced photocatalytic hydrogen evolution performance.

4. Conclusion

In summary, we developed a core–shell Fe_3O_4@PPy@Pt/Ag@I photocatalyst that integrates polyiodide-assisted charge transport with Pt–Ag alloy active sites within a conductive polymer matrix, guided by sustainability-driven design principles. The embedded polyiodide species establish efficient electron-transport pathways throughout the PPy network, enhancing charge separation and carrier mobility, while the Pt–Ag alloy nanodots optimize hydrogen adsorption–desorption energetics and interfacial electron transfer. By partially replacing Pt with Ag in the alloyed active sites, the catalyst achieves high activity with a reduced reliance on pure Pt, directly improving noble-metal utilization efficiency. The Fe_3O_4 magnetic core enables rapid recovery of the catalyst after the reaction, demonstrating operational recyclability. As a result of this synergistic regulation of charge transport, catalytic kinetics, and structural recoverability, Fe_3O_4@PPy@Pt/Ag@I achieves a 6.2-fold enhancement in hydrogen-evolution activity relative to Fe_3O_4@PPy@Pt. Although extended operation beyond 24 h leads to some structural changes, these observations provide guidance for future improvements in mechanical and chemical robustness. Overall, this work demonstrates a sustainability-oriented catalyst design strategy that simultaneously addresses charge-transport efficiency, noble-metal use, and catalyst recoverability, providing a practical pathway for resource-efficient and deployable conductive-polymer-based photocatalytic hydrogen-evolution systems.

Conflicts of interest

There are no conflicts to declare.

Data availability

The data that supports the findings of this study are available within the article.

Supplementary information (SI): XRD, XPS, Raman and FTIR analysis, calculation of mass activity, as well as stability testing of the photocatalysts. See DOI: https://doi.org/10.1039/d5su00533g.

References

1 S. W. Cao and J. G. Yu, Carbon-based H_2-production photocatalytic materials, *J. Photochem. Photobiol., C*, 2016, **27**, 72–99.

2 X. S. Li, D. Wang, S. J. Zha, Y. Chu, L. Pan, M. X. Wu, C. H. Liu, W. C. Wang, N. Mitsuzaki and Z. D. Chen, Active sites identification and engineering of M-N-C electrocatalysts toward oxygen reduction reaction, *Int. J. Hydrogen Energy*, 2023, **51**, 1110–1127.

3 X. X. Zou and Y. Zhang, Noble metal-free hydrogen evolution catalysts for water splitting, *Chem. Soc. Rev.*, 2015, **44**, 5148–5180.

4 S. Nandy, S. A. Savant and S. Haussener, Prospects and challenges in designing photocatalytic particle suspension reactors for solar fuel processing, *Chem. Sci.*, 2021, **12**, 9866–9884.

5 Y. Bai, C. L. Liu, Y. Y. Shan, T. T. Chen, Y. Zhao, C. Yu and H. Pang, Metal-Organic Frameworks Nanocomposites with Different Dimensionalities for Energy Conversion and Storage, *Adv. Energy Mater.*, 2022, **12**, 2100346.

6 X. Wu, S. W. Zuo, M. Qiu, Y. Li, Y. F. Zhang, P. F. An, J. Zhang, H. B. Zhang and J. Zhang, Atomically defined Co on two-dimensional TiO_2 nanosheet for photocatalytic hydrogen evolution, *Chem. Eng. J.*, 2021, **420**, 127681.

7 Y. Sun, J. K. Lin, W. W. Yang, X. Q. Chen, H. Y. Zhang, Y. Z. Liu, H. F. Qi, B. Y. Song, G. C. Zuo and S. G. Yang, Unraveling the Multifunctional Sites of Ag Single-Atom and Nanoparticles Confined Within Carbon Nitride Nanotubes for Synergistic Photocatalytic Hydrogen Evolution, *Small*, 2025, **21**, 2.

8 K. K. Das, S. Patnaik, S. Mansingh, A. Behera, A. Mohanty, C. Acharya and K. M. Parida, Enhanced photocatalytic

activities of polypyrrole sensitized zinc ferrite/graphitic carbon nitride n-n heterojunction towards ciprofloxacin degradation, hydrogen evolution and antibacterial studies, *J. Colloid Interface Sci.*, 2020, **561**, 551–567.

9 T. R. N. Kumar, P. Karthik and B. Neppolian, Polaron and bipolaron induced charge carrier transportation for enhanced photocatalytic H$_2$ production, *Nanoscale*, 2020, **12**, 14213–14221.

10 S. M. Abu-Sari, M. F. A. Patah, B. C. Ang and W. M. A. W. Daud, A review of polymerization fundamentals, modification method, and challenges of using PPy-based photocatalyst on perspective application, *J. Environ. Chem. Eng.*, 2022, **10**, 108725.

11 X. Wu, X. Yang, L. Yu and X. C. Chen, Imidazolium-based ionic liquids as proton reservoir for stable polyaniline cathode in zinc-iodine batteries, *Chem. Eng. J.*, 2024, **500**, 157437.

12 M. Ichikawa and H. Goto, Synthesis of a polyacetylene derivative bearing aspirin with chiral charge carrier "chiralions", *J. Macromol. Sci., Part A: Pure Appl. Chem.*, 2022, **59**, 53–58.

13 K. Komaba and H. Goto, Soliton excitations in liquid crystal polyacetylene, *Mol. Cryst. Liq. Cryst.*, 2020, **703**, 69–78.

14 D. Kumar, R. Tiwari, D. K. Verma, S. Yadav, K. Parwati, P. Adhikary and S. Krishnamoorthi, Isomeric polythiophene: a promising material for low voltage electronic devices, *Soft Matter*, 2024, **20**, 1293–1300.

15 L. N. Fan and X. C. Xue, A simple strategy to enhance electrical conductivity of nanotube-conjugate polymer composites *via* iodine-doping, *RSC Adv.*, 2015, **5**(95), 78104–78108.

16 Z. Küçükyavuz, S. Küçükyavuz and N. Abbasnejad, Electrically conductive polymers from poly(N-vinylimidazole), *Polymer*, 1996, **37**(15), 3215–3218.

17 E. Y. Jung, S. Khalil, H. Jang, H. O. Suleiman, J. Y. Kim, B. J. Shin, H. S. Tae and C. S. Park, Improvement of Electrical Conductivity of In Situ Iodine-Doped Polypyrrole Film Using Atmospheric Pressure Plasma Reactor with Capillary Electrodes, *Nanomaterials*, 2024, **14**, 468.

18 M. Rabia, E. Aldosari, A. M. Elsayed, A. Sanna and O. Farid, Highly porous network of tungsten (VI) oxide-iodide/polypyrrole nanocomposite photocathode for the green hydrogen generation, *Opt. Quantum Electron.*, 2024, **56**, 1068.

19 H. Ullah, A. A. Tahir and T. K. Mallick, Polypyrrole/TiO$_2$ composites for the application of photocatalysis, *Sens. Actuators, B*, 2017, **241**, 1161–1169.

20 M. Smiljanić, S. Panić, M. Bele, F. Ruiz-Zepeda, L. Pavko, L. Gašparić, A. Kokalj, M. Gaberšček and N. Hodnik, Improving the HER Activity and Stability of Pt Nanoparticles by Titanium Oxynitride Support, *ACS Catal.*, 2022, **12**, 13021–13033.

21 G. Gao, G. Zhu, X. Chen, Z. Sun and A. Cabot, Optimizing Pt-Based Alloy Electrocatalysts for Improved Hydrogen Evolution Performance in Alkaline Electrolytes: A Comprehensive Review, *ACS Nano*, 2023, **17**(21), 20804–20824.

22 Q. Li, Q. Wang, Y. Zeng, Y. Xu, X.-K. Gu and M. Ding, Ag-Pt Alloy Nanoparticles Modified Zn-Based Nanosheets for Highly Selective CO$_2$ Photoreduction to CH$_4$, *Adv. Funct. Mater.*, 2025, **35**, 2416975.

23 W. Liang, Y. Liu, W. Bian, W. Qin, Y. Wang, W. Guo, D. Li, H. Zeng, J. Zhong, Y. Sun, H. Lin and L. Jiang, Cascaded hot electron transfer within plasmonic Ag@Pt heterostructure for enhanced electrochemical reactions, *Sci. China Mater.*, 2023, **66**, 2227–2234.

24 P. Verma, K. Yuan, Y. Kuwahara, K. Mori and H. Yamashita, Enhancement of plasmonic activity by Pt/Ag bimetallic nanocatalyst supported on mesoporous silica in the hydrogen production from hydrogen storage material, *Appl. Catal., B*, 2018, **223**, 10–15.

25 H. Fei, J. Dong, M. J. Arellano-Jiménez, G. Ye, N. D. Kim, E. L. G. Samuel, Z. Peng, Z. Zhu, F. Qin, J. Bao, M. J. Yacaman, P. M. Ajayan, D. Chen and J. M. Tour, Atomic Cobalt on Nitrogen-Doped Graphene for Hydrogen Generation, *Nat. Commun.*, 2015, **6**, 8668.

26 M. Hong and A. Jo, Improved Electrochemical Surface Area Measurement of Platinum Using a Potential Holding Strategy, *Electrochim. Acta*, 2025, **540**, 147249.

27 Z. Li, B. Tian, W. Y. Zhang, X. Q. Zhang, Y. Q. Wu and G. X. Lu, Enhancing photoactivity for hydrogen generation by electron tunneling via flip-flop hopping over iodinated graphitic carbon nitride, *Appl. Catal., B*, 2017, **204**, 33–42.

28 L. A. Mancera, A. Groß and R. J. Behm, Stability, electronic properties and CO adsorption properties of bimetallic PtAg/Pt(111) surfaces, *Phys. Chem. Chem. Phys.*, 2024, **26**, 18435–18448.

29 L. Y. Xiao, Z. L. Wang and J. Q. i. Guan, Optimization strategies of high-entropy alloys for electrocatalytic applications, *Chem. Sci.*, 2023, **14**, 12850.

30 Q. Tang, L. Guo, T. Jin, S. Shan, Q. Wang, J. Wang, B. Pan, Z. Li, Y. Chai and F. Chen, Stable Strain State of Single-Twinned AgPdF Nanoalloys under Formate Oxidation Reaction, *Small Struct.*, 2023, **4**, 2300110.

31 S. Kosame, M. Joseph Josline, J.-H. Lee and H. Ju, Anomalous spectral shift of localized surface plasmon resonance, *Nanoscale Adv.*, 2024, **6**, 2636.

32 I. Lee, J. Y. Park, K. Hong, J. H. Son, S. Kim and J.-L. Lee, The effect of localized surface plasmon resonance on the emission color change in organic light emitting diodes, *Nanoscale*, 2016, **8**, 6463.